# Mapping variations in weight percent silica measured from multispectral thermal infrared imagery—Examples from the Hiller Mountains, Nevada, USA and Tres Virgenes-La Reforma, Baja California Sur, Mexico

Simon J. Hook[a,*], Jane E. Dmochowski[b], Keith A. Howard[c], Lawrence C. Rowan[d], Karl E. Karlstrom[e], Joann M. Stock[b]

[a]Mail Stop 183-501, Jet Propulsion Laboratory, California Institute of Technology, Pasadena CA 91009, USA
[b]Campus, California Institute of Technology, Pasadena CA 91125, USA
[c]U.S. Geological Survey, Menlo Park, CA 94025, USA
[d]U.S. Geological Survey, National Center, Reston, VA 20192, USA
[e]Department of Earth and Planetary Sciences, University of New Mexico, Albuquerque, NM 87131, USA

## Abstract

Remotely sensed multispectral thermal infrared (8–13 μm) images are increasingly being used to map variations in surface silicate mineralogy. These studies utilize the shift to longer wavelengths in the main spectral feature in minerals in this wavelength region (reststrahlen band) as the mineralogy changes from felsic to mafic. An approach is described for determining the amount of this shift and then using the shift with a reference curve, derived from laboratory data, to remotely determine the weight percent $SiO_2$ of the surface. The approach has broad applicability to many study areas and can also be fine-tuned to give greater accuracy in a particular study area if field samples are available. The approach was assessed using airborne multispectral thermal infrared images from the Hiller Mountains, Nevada, USA and the Tres Virgenes-La Reforma, Baja California Sur, Mexico. Results indicate the general approach slightly overestimates the weight percent $SiO_2$ of low silica rocks (e.g. basalt) and underestimates the weight percent $SiO_2$ of high silica rocks (e.g. granite). Fine tuning the general approach with measurements from field samples provided good results for both areas with errors in the recovered weight percent $SiO_2$ of a few percent. The map units identified by these techniques and traditional mapping at the Hiller Mountains demonstrate the continuity of the crystalline rocks from the Hiller Mountains southward to the White Hills supporting the idea that these ranges represent an essentially continuous footwall block below a regional detachment. Results from the Baja California data verify the most recent volcanism to be basaltic–andesite.
© 2005 Elsevier Inc. All rights reserved.

Keywords: Silica; Weight percent; Infrared imagery; MODIS/ASTER Airborne Simulator (MASTER)

## 1. Introduction

Numerous studies have demonstrated the usefulness of remotely sensed data for geological mapping. These studies typically utilize data from the visible through shortwave infrared (0.4–2.5 μm) part of the electromagnetic spectrum, because high spatial resolution datasets covering this wavelength range are available globally. The spectral features observed in rocks in this wavelength region are primarily due to iron oxide, carbonate and hydroxyl-bearing minerals. Far fewer studies have focused on the use of remotely sensed data covering the thermal infrared (8–13 μm) part of the electromagnetic spectrum where spectral features related to differences in Si–O bonding of silicate minerals can be observed. Differences in Si–O bonding are manifest as shifts in the position of the minimum in the emissivity spectra of rocks in the thermal infrared wavelength region.

---

* Corresponding author.
  E-mail address: Simon.J.Hook@jpl.nasa.gov (S.J. Hook).

Variations in silicate mineralogy are particularly useful for geologic mapping because they are an important criterion in classifying and interpreting igneous rocks, as well as sedimentary and metamorphic rocks derived from them. Studies utilizing thermal infrared data have demonstrated that it is possible to distinguish between rock types based on differences in silicate mineralogy (e.g. Abrams et al., 1991; Cudahy et al., 1999; Hook et al., 1994; Lahren et al., 1988; Sabine et al., 1994; Watson et al., 1996). Such qualitative studies are useful but do not provide a quantitative basis for comparing similar lithotypes between regions. More recently, two other more quantitative approaches have been studied; these are mineral mapping using mixture modeling and weight percent silica estimation using Gaussian fitting. Mineral mapping using mixture modeling has been shown to work well with data from the visible shortwave infrared part of the electromagnetic spectrum where instruments are available with many narrow spectral channels such as the Airborne Visible Infrared Imaging Spectrometer (AVIRIS). These instruments typically have 200+ narrow spectral channels allowing the detection of absorption features related to the presence of specific minerals (Neville et al., 2003; Plaza et al., 2004). Mixture modeling has been applied to thermal infrared data from airborne and spaceborne instruments but specific mineral identification is typically limited due to the small number and broad spectral coverage of the thermal infrared channels on current instruments (Gillespie et al., 1992; Bandfield, 2002; Ramsey & Christensen, 1998). An alternative to mineral mapping by mixture modeling is the estimation of weight percent silica by Gaussian fitting. This approach utilizes a shift in the emissivity minimum to estimate the weight percent $SiO_2$ of igneous rocks. Both approaches, mineral mapping by mixture modeling and the estimation of weight percent silica by Gaussian fitting, are valuable with data from instruments with a limited number of spectrally broad thermal infrared channels. Given an

instrument with more channels and adequate signal to noise improved mineral maps could be produced and other fitting approaches explored for the estimation of the weight percent silica. Weight percent silica estimation was first used by Gillespie (1986) and Sabine et al. (1994). These authors customized the technique for their sites and as a result their approach is not readily applicable to other study areas. Their work was also limited by calibration problems associated with the available instrumentation. The present study describes a general method for estimating silica content from multispectral thermal infrared data with broad applicability to many study areas that can be fine-tuned for a particular area for greater accuracy if field samples are available. The coefficients necessary for estimating weight percent $SiO_2$ are derived for the newer airborne and spaceborne instruments including the Advanced Spaceborne Thermal Emission and Reflectance radiometer (ASTER) and the Moderate Resolution Imaging Spectrometer (MODIS) /ASTER airborne simulator (MASTER), respectively.

This study utilizes data acquired by the MASTER instrument. MASTER is a 50-channel airborne-imaging spectrometer (Hook et al., 2001) with 25 channels in the visible to shortwave infrared (0.4–2.4 μm), 15 channels in the mid infrared (MIR, 3.1–5.3 μm) and 10 channels in the thermal infrared (TIR, 7.8–12.9 μm). The MASTER data used in this study were acquired on December 2, 1998 and April 29, 1999 from a Beechcraft B200 aircraft and have a spatial resolution of 15 m and 5.5 m, respectively for the Hiller Mountains and La Reforma study sites. Only the thermal infrared channels of MASTER covering the 7–13 μm region were used in this study (Fig. 1).

First, the theoretical framework for remote sensing of silicate rocks in the thermal infrared region is described and then the technique for deriving the weight percent $SiO_2$ of igneous rocks using thermal infrared data. This discussion is
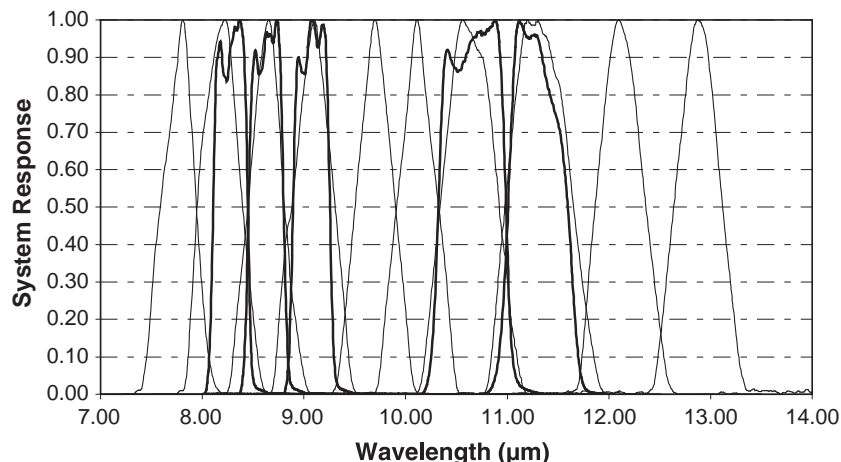


Fig. 1. System response functions for the MASTER and ASTER thermal infrared channels. The MASTER system response functions are for August 1998. ASTER system response functions shown in bold.

followed by a description of the geology of the study areas and the data processing procedure. The processed data are then interpreted, and the algorithm for determining the weight percent $SiO_2$ is assessed. Finally, the approach is summarized and conclusions are drawn.

## 2. Theoretical framework

The reflectance and emissivity spectra of minerals exhibit diagnostic features at various wavelengths which provide a means for their remote discrimination and identification. These features are caused by the interaction of electromagnetic energy with the atoms and molecules that make up the mineral. Light of infrared frequencies can generally promote molecules from a vibrational ground state to various excited states. Different Si–O bonded structures vary in their interaction with thermal infrared light (8–13 μm). The region in which the Si–O spectral features related to Si–O stretching occur is referred to as a reststrahlen band. The emissivity minimum for this band occurs at shorter wavelengths (8.5 μm) for framework silicates (quartz, feldspar) and progressively longer wavelengths for silicates having sheet, chain, and isolated tetrahedral structure (Hunt, 1980). Because framework silicates dominate felsic igneous rocks and chain silicates dominate mafic igneous rocks, in general, the minimum of the Si–O stretching region moves to longer wavelengths as the weight percent $SiO_2$ decreases (Fig. 2).

## 3. Determination of relationship between wavelength minimum and weight percent silica

In order to take advantage of the relationship of the systematic shift in the minimum in the Si–O stretching region to igneous rock composition it is necessary to establish a technique for the determination of the minimum as well as the most suitable chemical parameter. Gillespie (1986) determined the minimum using a Gaussian function and Sabine et al. (1994) expanded on Gillespie's work by evaluating the relationship between the Gaussian minimum and a variety of chemical and modal parameters. The Gaussian approach was utilized due to the limited number of spectral bands. Sabine et al. found the highest correlation was between $SiO_2$ content and the Gaussian minimum. The Gaussian minimum for the samples used by Sabine et al. was determined from emissivity spectra derived from Thermal Infrared Multispectral Scanner (TIMS) data. The TIMS instrument was a multispectral scanner that acquired 6 channels of data in the thermal infrared (8–13 μm) wavelength region. The TIMS data used by Sabine et al. were obtained over the Desolation Wilderness area of the northern Sierra Nevada, California. The rocks exposed there are primarily granitoids and range in weight percent $SiO_2$ from 50% to 70%. The TIMS instrument was the forerunner to the MASTER instrument which has 10 channels in the wavelength region equivalent to TIMS. In order to determine the weight percent $SiO_2$, the emissivity minimum from the TIMS data was regressed against the weight percent $SiO_2$ obtained from field samples. Because the image data were regressed against the weight percent silica measurements any artifacts in the original TIMS spectra were incorporated in the relationship between the minimum and $SiO_2$ content, limiting the general applicability of the technique to other areas or datasets derived from other instruments. In order to determine if this relationship could be related to a wide range in $SiO_2$ content as well as the applicability of the technique to igneous rock spectra in general, the relationship was evaluated using the spectral data for igneous rocks in the ASTER spectral library (http://speclib.jpl.nasa.gov) and this evaluation is discussed below. The ASTER spectral library includes hemispherical reflectance
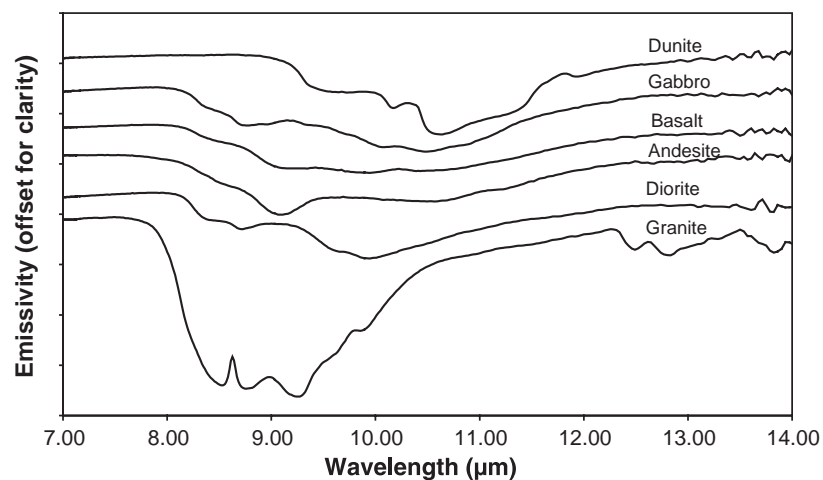


Fig. 2. Laboratory hemispherical reflectance spectra of a variety of igneous rocks ranging in composition from ultramafic to felsic. Spectra obtained from the ASTER Spectral Library.
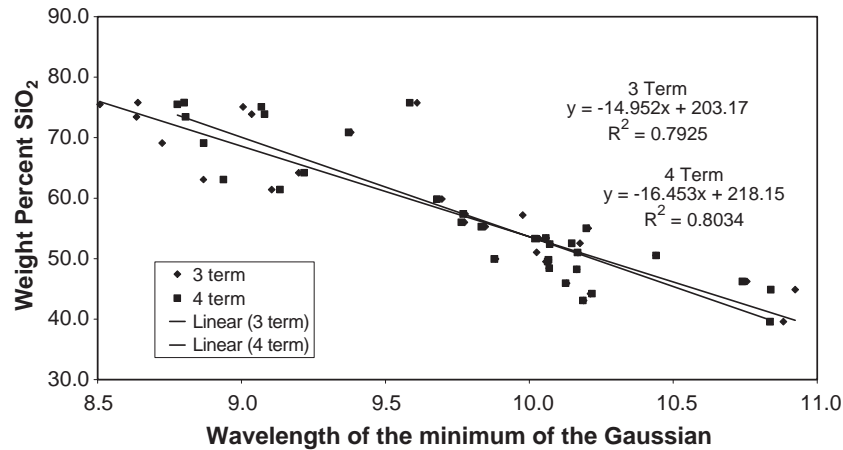
Fig. 3. Gaussian-fit minimum values derived from the library spectra plotted against their corresponding weight percent $SiO_2$ values. Minimum values were obtained by fitting a 3- and 4-term Gaussian function to laboratory hemispherical reflectance spectra of igneous rocks. The spectra and weight percent $SiO_2$ values were obtained from the ASTER Spectral Library.

spectra from 35 igneous rock samples with weight percent $SiO_2$ contents ranging from 43% to 76%.

The emissivity minimum of each laboratory spectrum was determined with a 3- and 4-term Gaussian function:

$$f(x) = A_0 e^{\frac{-z^2}{2}} \quad (3 - \text{term})$$

$$f(x) = A_0 e^{\frac{-z^2}{2}} + A_3 \quad (4 - \text{term})$$

where:

$$z = \frac{x - A_1}{A_2} \quad \text{and}$$

$x =$ the emissivity values for each spectrum.

$A_0$ through $A_3$ are the fit values for the Gaussian function $f(x)$. The four terms of the Gaussian function correspond to the amplitude, position of the minimum value, area enclosed by the function and an offset, respectively.

Sabine et al. (1994) determined a linear relationship between the minimum wavelength (obtained by fitting a 3-term Gaussian function [or model] to TIMS data) and the

weight percent $SiO_2$ (obtained by chemical analysis of samples from locations in the TIMS imagery). Sabine et al. also showed fit values of the Gaussian to the field sample spectra. In this study Gaussian-fit values were calculated for the laboratory spectra and the laboratory spectra were convolved with the system response of two instruments (MASTER and ASTER) as well as various MASTER channel combinations producing several datasets of Gaussian-fit values. The best Gaussian fit was obtained using a least squares approach. The position coefficient of the fit ($A_1$ term) from each sample in each dataset was plotted against its corresponding weight percent $SiO_2$ value determined by chemical analysis and a least squares fit performed on each dataset. Fig. 3 shows a plot of the minimum obtained using 3- and 4-term Gaussian fits, of the full resolution emissivity spectra covering the 8–12 μm wavelength region versus the corresponding weight percent $SiO_2$ values. Table 1 lists the coefficients obtained from performing least squares fits on the various datasets including the correlation coefficients. Evaluation of various channel combinations is important because certain channels are more strongly affected by the atmosphere and can

Table 1
Results from fitting the ASTER spectral library igneous rocks with a 3-term and 4-term Gaussian model

| Sample set | 3-Term Gaussian model | | | | 4-Term Gaussian model | | | |
|---|---|---|---|---|---|---|---|---|
| | $N$ | m | c | $R^2$ | $N$ | m | c | $R^2$ |
| 7–14 μm (full resolution) | 35 | −44.161 | 513.13 | 0.6617 | 35 | −41.326 | 482.81 | 0.7082 |
| 8–12 μm (full resolution) | 35 | −14.952 | 203.17 | 0.7925 | 33 | −16.453 | 218.15 | 0.8034 |
| MASTER 41–50 channels (7.737–12.888 μm) | 35 | −26.228 | 322.24 | 0.8216 | 35 | −25.981 | 319.47 | 0.8307 |
| MASTER 41–49 channels (7.737–12.131 μm) | 35 | −28.655 | 343.6 | 0.7705 | 35 | −27.806 | 334.74 | 0.7867 |
| MASTER 42–50 channels (8.153–12.888 μm) | 35 | −0.3802 | 57.46 | 0.4719 | 35 | −0.0017 | 56.318 | 0.105 |
| MASTER 42–49 channels (8.153–12.131 μm) | 35 | −7.8321 | 131.52 | 0.71 | 34 | −10.9 | 162.29 | 0.7755 |
| MASTER 43–48 channels (8.604–11.331 μm) | 35 | −0.8772 | 62.367 | 0.4846 | 35 | −0.568 | 60.982 | 0.2565 |
| ASTER (8.287–11.289 μm) | 35 | −7.5624 | 131.19 | 0.5832 | 35 | −10.548 | 160.25 | 0.662 |
| ASTER (8.287–11.289 μm) excluding ultramafics | 32 | −14.27 | 194.76 | 0.7581 | 32 | −16.203 | 213.97 | 0.7615 |

$N$=number of samples; $m$ and $c$=coefficients for linear fit ($y=mx+c$) of minimum versus wt.% silica; $R^2$=correlation coefficient. A value of $N$ less than 35 indicates that the Gaussian model failed to adequately fit (match) certain spectra (failed spectra are not included in calculating the overall fit). Wavelength range shown is from centroid value of first channel to centroid value of last channel.
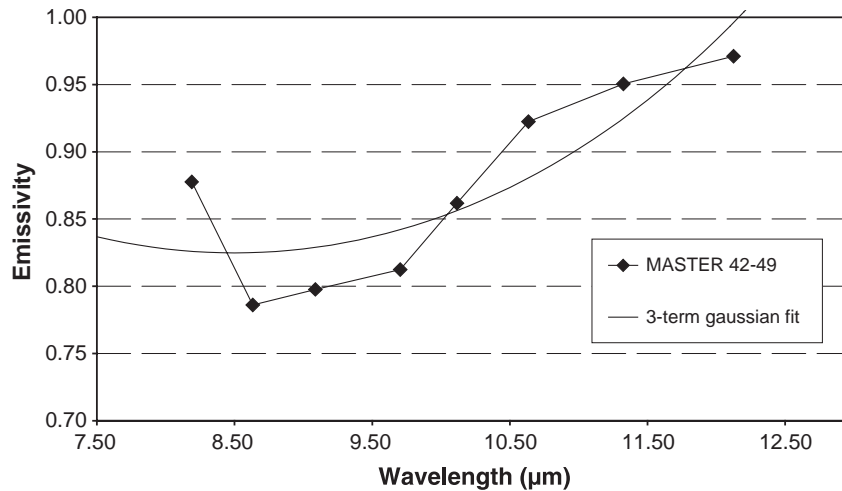
Fig. 4. Gaussian function (3-term) fitted to a library spectrum of quartz monzonite convolved to MASTER channels 42–49 illustrating the effect of excluding the longest wavelength channel on the fit.

be difficult to correct. Often it is better to exclude these channels if they cannot be adequately corrected. Otherwise the assumption that the spectrum can be treated as a Gaussian will be invalid since the emissivity spectrum will contain residual effects from the atmospheric correction. This point is discussed further in the subsequent section on data processing.

The highest correlation coefficient was obtained using the library data convolved to the 10 MASTER channels (41–50) and fit with a 4-term Gaussian function ($r^2$=0.83). The results obtained using the 3-term Gaussian fit were only slightly worse ($r^2$=0.82) as was the case for the other band combinations (Table 1), except the 42–50 and 43–48 channel combinations which are discussed subsequently. This result supports using the 3-term Gaussian fit for most image manipulations where computational speed is important. (The current implementation of the algorithm which has not been optimized takes several hours on a few thousand line image). The 3-term fit to the library data

convolved to the 10 MASTER channels was similar to the fit for the full resolution library data for the 8–12 μm wavelength region ($r^2$=0.79). These fits are better than the 3-term fit to the full resolution library data for the 7–14 μm region ($r^2$=0.66). This is due to the fact that the Si–O stretching region, fitted by the Gaussian model, is between 8 and 12 μm and by including a wider wavelength range, the values outside the stretching region diminish the ability of the Gaussian model to fit the region correctly. Further examination of Table 1 indicates that if a similar analysis is performed using MASTER channels 41–49 or 42–49 the correlation coefficients are similar to using channels 41–50. If channels 42–50 or 43–48 are used the correlation coefficients are much worse (channels 42–50, $r^2$=0.47; channels 43–48, $r^2$=0.48) and can be explained by examining plots in which the Gaussian model is superimposed on the original library spectra (Figs. 4–6). If MASTER channels 42–49 are used (Fig. 4), the fit is equally influenced by the values outside the Si–O stretching region,
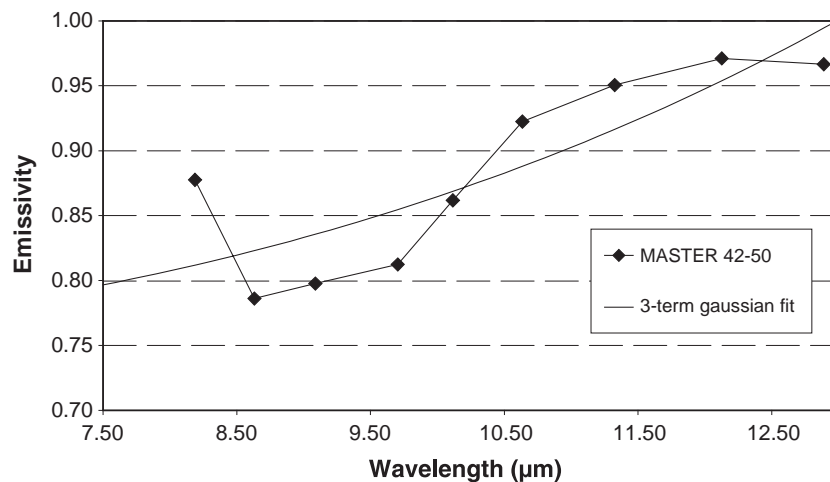


Fig. 5. Gaussian function (3-term) fitted to a library spectrum of quartz monzonite convolved to MASTER channels 42–50 illustrating the influence of the longest wavelength channel (channel 50) on the fit.
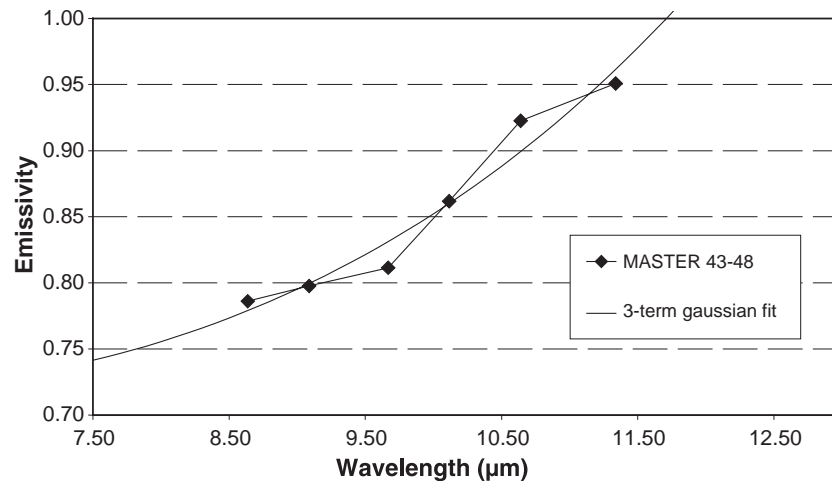
Fig. 6. Gaussian function (3-term) fitted to a library spectrum of quartz monzonite convolved to MASTER channels 43–48 illustrating the effect of not fully encompassing the Si–O stretching region on the fit. Emissivity information for channels 41–42 and 49–50 was intentionally left out to illustrate the effect. Minimum obtained using channels 42–49 was 8.5 μm.

whereas if channels 42–50 are used the fit is more strongly influenced by the longer wavelength channels outside the Si–O stretching region (Fig. 5). If MASTER channels 43–48 are used, the wavelength range does not fully encompass the Si–O stretching region and the ability of the Gaussian function to correctly locate the minimum of the full Si–O stretching region is reduced (Fig. 6).

Table 1 also provides the coefficients for the library data convolved to the ASTER channels, since these data are available globally, albeit with a low spatial resolution (90 m), and the ability to map weight percent $SiO_2$ with these data is highly desirable. The correlation coefficient for the library data convolved to the ASTER wavelengths and fit by a 3-term Gaussian function is 0.58 (Table 1). The lower correlation coefficient for ASTER as opposed to the 10-channel MASTER data results from the ASTER channels not fully encompassing the Si–O stretching region. The igneous rocks most strongly affected by this limitation are ultramafic rocks. If the results from ultramafic rocks are excluded, the correlation coefficient increases to 0.76 (Table 1).

It should also be noted that the channel positions of some instruments (e.g. MASTER) shift over time and require frequent calibration (Hook et al., 2001). Large shifts may require recalculation of the regression coefficients. In this paper the system response files for MASTER were taken to match the MASTER overflight. The MASTER system response files are available from the MASTER web site: http://masterweb.jpl.nasa.gov.

## 4. Geologic setting

Two study sites were selected to test mapping the weight percent $SiO_2$: the Hiller Mountains, Nevada, USA and the Tres Virgenes-La Reforma area, Baja California Sur, Mexico. Both sites are ideal for testing this approach due to the low rainfall, sparse vegetation cover, and a wide range of rock compositions. These study sites should allow a good assessment of the approach in semi-arid terrains with good exposure; further studies are required to assess the approach in other more heavily weathered or vegetated regions. The Hiller Mountains expose a varied series of Proterozoic gneisses and granitoids, and surrounding alluvial detritus, limestone, and basalt. The Proterozoic rocks mostly are veneered by dark desert varnish, which on color aerial photographs or distant visual views obscures the lithologic differences between rock types. Remoteness and ruggedness of parts of the area make application of aerial photographs and other remotely sensed imagery helpful in geologic mapping, but distinctions between rock units are subtle at best in the visible parts of the spectrum.

The La Reforma caldera exposes a varied series of Quaternary and Tertiary volcanic rocks including basaltic–andesite flows; intracaldera rhyolite ash flow tuffs and andesitic, dacitic, and rhyolite lavas; an intrusive body of diorite porphyry; and detritus derived from the rocks listed above.

### 4.1. Hiller Mountains

The Hiller Mountains area includes part of the Gold Butte structural block at the south end of the Virgin Mountains in the northeastern part of Clark County, Nevada, USA. Lake Mead wraps southward around the Hiller Mountains, with the narrow Virgin Canyon arm of the lake separating the Hiller Mountains from the White Hills to the south. Howard et al. (2003), Longwell et al. (1965), and Volborth (1962) mapped the geology of the study area and Fryxell et al. (1992) mapped the area immediately to the north.

The Virgin Mountains form a series of Precambrian-cored fault blocks that make up the first major ranges of the Basin and Range Province west of the Colorado Plateau.

The present structure reflects Miocene extensional tectonism (Wernicke et al., 1984) and the interplay of north–south striking moderate- to low-angle normal faults and NE-striking left-lateral faults that make up the northeast extension of the Lake Mead fault zone. The strike-slip faults segment the Virgin Mountains into distinct structural and lithologic domains (Beard, 1996; Duebendorfer et al., 1998), each with somewhat different Tertiary extensional structures and different dominant rock types and mineral deposits. East–west extension of 15 km is recorded by the geometry of west-dipping normal faults cutting east-dipping Paleozoic, Mesozoic, and Tertiary strata immediately north and east of the Gold Butte block (Brady et al., 2000). The Paleozoic and Mesozoic formations correlate with strata exposed in Grand Canyon and Zion National Parks to the east and northeast, respectively.

The Gold Butte block consists of 400 km$^2$ of Paleoproterozoic amphibolite- to granulite-grade gneisses and cross-cutting plutons of the Mesoproterozoic Gold Butte Granite. These rocks are nonconformably overlain on the east side of the block 5 km northeast of the study area by E-dipping (50–60°)Paleozoic strata. High-grade Paleoproterozoic rocks at the west side of the block are chloritized (including chlorite breccia) and mylonitic, supporting the presence of a W-dipping low-angle extensional detachment fault bounding the west side of the Gold Butte block (Brady et al., 2000; Fitzgerald et al., 1991; Fryxell et al., 1992). The rocks of the Gold Butte block track southward with little interruption into the Hiller Mountains and Arizona's White Hills. Based on the tilted Paleozoic rocks and study of the Proterozoic basement, Fryxell et al. (1992) and Wernicke and Axen (1988) proposed that the Gold Butte block represents an east-tilted crustal section that exposes crustal depths to 15 km (half of the present crustal thickness) or more. Mineral dating by U–Pb, 40Ar/39Ar, fission-track, and (U–Th)/He show that cooling ages decrease westward in the block, in support of its interpretation as an oblique depth section (Bernet et al., 2002; Fitzgerald et al., 1991; Reiners, 2002; Reiners et al., 2000). The dating furthermore documents that much of the block was quenched below 100 °C at 15–16 Ma. This timing is consistent with the stratigraphically determined timing of westward-directed extensional tectonic unroofing and eastward block tilting (Beard, 1996; Duebendorfer & Sharp, 1998).

High-grade gneisses, including garnet-cordierite-sillimanite gneiss, amphibolite, foliated granitoids, and ultramafic rocks, underlie two thirds of the Gold Butte block and Hiller Mountains (Fryxell et al., 1992; Howard et al., 2003; Thomas et al., 1988; Volborth, 1962). Dating of gneisses and granitoids in surrounding regions of Arizona and to the southwest in the Mojave Desert suggests that supracrustal protoliths about 1.75–1.8 Ga were intruded by plutons and metamorphosed between 1.76 and 1.68 Ga (Chamberlain & Bowring, 1990; Duebendorfer et al., 2001; Hawkins et al., 1996; Ilg et al., 1996; Wooden & Miller, 1990). Paleoproterozoic rocks are cut by a voluminous assemblage (one third of the Gold Butte block) of 1.4 Ga Gold Butte Granite, part of the so-called "anorogenic" granites of the North American Southwest (Anderson, 1983). Plutons of the Gold Butte Granite are post tectonic relative to the foliated gneisses and their granulite to upper amphibolite facies metamorphism.

Proterozoic structures include a pervasive shallow-dipping foliation and upright NW-trending folds of the foliation. Both of these generations of deformation predated the 1.4 Ga granites, with no new recognized deformation associated with the 1.4 Ga event (Volborth, 1962).

## 4.2. La Reforma Caldera

The La Reforma caldera is on the east coast of Baja California, Mexico at 27.5° N latitude, just south of the border between Baja California Norte and Baja California Sur. The region, including three volcanic systems—La Reforma caldera to the east, El Aguajito caldera to the north, and the Tres Virgenes volcanoes to the southwest—is seismically active (Guerrero-Guadarrama, 1998). Cretaceous granitic rocks probably form the basement of this region, as evidenced by several outcrops within the volcanic centers (Sawlan, 1981). The volcanism is compositionally somewhat anomalous, as it has the major and trace element characteristics of typical calcalkaline arc lavas (Sawlan, 1986). The volcanism is related not to an active subduction zone, but rather to extensional deformation associated with the formation of the Gulf of California (Colletta & Angelier, 1981; Sawlan, 1981; Sawlan & Smith, 1984). Subduction in this region, responsible for forming the Comondú volcanics to the south and west of this region, halted approximately 12.5–11 Ma (Mammerickx & Klitgord, 1982).

The La Reforma volcanic complex has been dated ca. 1.09 Ma (Schmidt, 1975). However, the geologic history of the complex is not well understood. La Reforma has a typical caldera morphology, with a ring escarpment approximately 10 km in diameter and a central block (surrounded by associated silicic domes), which stands 700 m above the caldera margins. Pyroclastic and lava outflow sheets flank the rim of the caldera and can be seen in the deep canyon walls. Demant (1984), Demant and Ortlieb (1981) interpreted the central block of La Reforma to be a block of Miocene Comondú lavas uplifted by piston-like movement. This contrasts with the interpretation by Schmidt (1975), who described the feature not as a caldera, but as a system of tectonic blocks, and Walker et al. (1992), who described the complex as an updomed structure that has been circularly eroded. In fact, La Reforma likely is a caldera, due to its composition and morphology. The central dome is not a block of Miocene Comondú volcanics, but has recently been shown to be composed of welded ash-flow tuffs and lavas (Hausback et al., 2000), more typical of a caldera resurgent dome.

## 5. Data processing

MASTER data are provided as calibrated-at-sensor radiance data in hierarchical data format (HDF). The algorithm for mapping weight percent $SiO_2$ uses the surface emissivity as input, which requires that the surface emissivity be extracted from the radiance-at-sensor data. This step involved correcting the data for atmospheric effects and performing a temperature and emissivity (T/E) separation. In addition, a decorrelation stretch image was produced from the atmospherically corrected data to aid in interpreting the weight percent $SiO_2$ map. A decorrelation stretch image is commonly used for interpreting thermal infrared data, as it enhances emissivity variations, related to differences in composition, and displays them as color differences while maintaining temperature variations, related to differences in topography, and displaying them as differences in brightness (Gillespie et al., 1986).

The atmospheric component to the radiance at sensor was removed using the MODTRAN radiative transfer model (Berk et al., 1989). MODTRAN derives values for the atmospheric correction based on an input atmospheric profile, which may be obtained from default profiles in MODTRAN, or the profile may be modified or replaced with local atmospheric data. For the Hiller Mountains MASTER dataset a local atmospheric profile was available from the launch of an atmospheric sounding balloon at the same time as the MASTER overpass. A detailed description of these data is available in Hook et al. (2001). For the MASTER data acquired over the Tres Virgenes-La Reforma area no local atmospheric profiles were available and numerical forecast profiles from the National Center for Environmental Prediction (NCEP) were used instead. The NCEP produces global model values on a $1° \times 1°$ grid at 6 h intervals. Because the site does not lie on a grid node the NCEP values were interpolated in time and space to coincide with the aircraft overpass.

In order to assess the atmospheric correction for the Hiller Mountains, the kinetic temperature of an area of water was examined. Water has a known emissivity in the thermal infrared and, therefore, if the atmospheric correction is performed correctly and the known emissivities are used, the water temperatures derived for each channel should be constant. Initial examination indicated there was approximately 2 °C of spread in the water temperatures for the central eight channels. This spread was attributed to an incomplete correction for water vapor and ozone. The NCEP model profile does not include ozone and therefore the default profile included with MODTRAN is used. Previous work has shown that the temperatures derived from any channels that impinge on the main ozone absorption band do not typically agree with the temperatures derived from the channels either side of the ozone band. This temperature difference has been attributed to an incorrect adjustment for the amount of ozone between the aircraft scanner and the surface (Hook et al., 1992). Although satellite instruments have been used to estimate the amount of ozone present, these instruments do not sense the amount of ozone in the lower troposphere which is quite variable. These data were acquired from an aircraft flying in the lower troposphere. Therefore the amount of ozone and water vapor in the atmospheric profile was adjusted to minimize the spread of the derived temperatures in the central eight channels. Using this approach it was possible to reduce the spread to less than 1 °C (Table 2). After adjustment, the values for channel 41 were cooler than the other channels. Complete correction of the channel 41 data was not possible without increasing the overall spread between channels. Atmospheric correction of channel 41, centered on 7.77 μm, is particularly difficult because this wavelength region is strongly influenced by atmospheric water vapor. Initially it was hoped that it would be possible to correct this channel given the dry atmospheres above these targets but it was not possible using this approach. Therefore, channels 42–49 were used to determine weight percent $SiO_2$ for the Hiller Mountains MASTER dataset. Note, channel 50 was not included in the determination as it would have adversely affected the fitting procedure as discussed in the previous section. A similar approach was taken for correcting the MASTER data over the Tres Virgenes-La Reforma volcanic region.

After atmospheric correction, the emissivity information was extracted from channels 42–49 using the TES technique (Gillespie et al., 1998). In the TES technique, the difference

Table 2
Surface kinetic temperature values derived from the MASTER data for the Hiller Mountains from a block of 468 pixels over Lake Mead

| Channel | Central wavelength (μm) | Emissivity | Min | Max | Mean | Standard deviation |
|---|---|---|---|---|---|---|
| 41 | 7.766 | 0.982 | 1.350 | 18.190 | 10.626 | 3.007 |
| 42 | 8.188 | 0.983 | 15.440 | 18.290 | 16.779 | 0.467 |
| 43 | 8.632 | 0.984 | 16.190 | 17.740 | 16.927 | 0.279 |
| 44 | 9.087 | 0.985 | 15.670 | 17.230 | 16.386 | 0.232 |
| 45 | 9.703 | 0.987 | 15.240 | 17.320 | 16.270 | 0.325 |
| 46 | 10.116 | 0.989 | 15.270 | 16.990 | 16.175 | 0.297 |
| 47 | 10.635 | 0.991 | 15.430 | 17.100 | 16.280 | 0.295 |
| 48 | 11.325 | 0.990 | 15.190 | 17.410 | 16.345 | 0.392 |
| 49 | 12.125 | 0.984 | 13.370 | 19.240 | 16.012 | 0.958 |
| 50 | 12.888 | 0.975 | 9.610 | 23.680 | 16.024 | 1.986 |
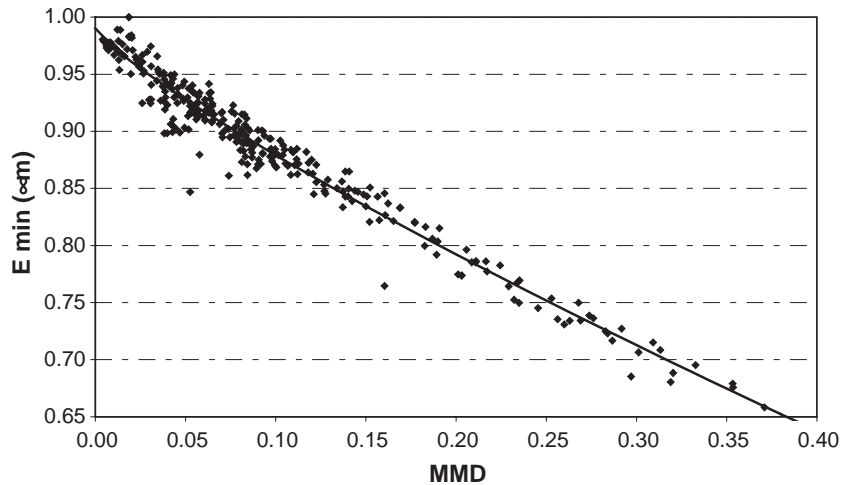
Fig. 7. Empirical calibration curve of the difference between the maximum and minimum (MMD) of the beta residuals and the minimum emissivity. The calibration curve was developed using data from the ASTER spectral library.

between the maximum and minimum beta residual of a given pixel (MMD) is used to determine the unknown minimum emissivity of the pixel using a calibration curve developed from laboratory spectra. The MMD is dependent on the channel placement for a given instrument and therefore a calibration curve was developed specifically for the eight central MASTER channels (Fig. 7). The initial curve developed for ASTER by Gillespie et al. (1998) used 86 laboratory spectra in the ASTER spectral library. Subsequently, additional samples have been added to the ASTER library, which permitted the regression for the MASTER equations to be developed using 314 spectra. The names of the sample groups used for the regression from the ASTER spectral library are included in the caption for Table 3 together with the regression coefficients for ASTER and MASTER.

The emissivity data for each pixel were then fitted with a 3-term Gaussian function using a minimum least squares

approach and the minimum of the Gaussian function used with the appropriate coefficients from Table 1 to determine the weight percent $SiO_2$. These data were used to produce weight percent $SiO_2$ maps of the study areas.

Table 3
Regression coefficients used with the TES technique

| Instrument | Count | Channels | Coefficients | | | $r^2$ |
|---|---|---|---|---|---|---|
| | | | a | b | c | |
| MASTER | 8.00 | 42–49 | 0.990 | 0.757 | 0.834 | 0.960 |
| MASTER | 10.00 | 41–50 | 1.001 | 0.761 | 0.812 | 0.970 |
| ASTER | 5.00 | 10–14 | 0.994 | 0.687 | 0.737 | 0.983 |

Equation: $Y=a-b*x^c$

The coefficients were calculated for MASTER channels 41–50 and 42–49. The ASTER spectral library datasets used for the regressions were: JHU lunar, JHU igneous-solid, JHU metamorphic-powders (500–1500 μm particle size), JHU sedimentary-powders (500–1500 μm particle size), JHU soils, JHU vegetation, JHU water, JPL soils, USGS borates, USGS carbonates, USGS chlorides, USGS sulfides, USGS igneous-solid, USGS metamorphic-solid and USGS sedimentary-solid. The coefficients in the table above are the least squares best fits to plots of the emissivity minimum (emin) versus the difference between the maximum and minimum (MMD) emissivity for the library spectra (see Fig. 7 for a plot of a fit to the MASTER data). The emin–MMD follows a simple power law. Values for ASTER taken from Gillespie et al. (1998).
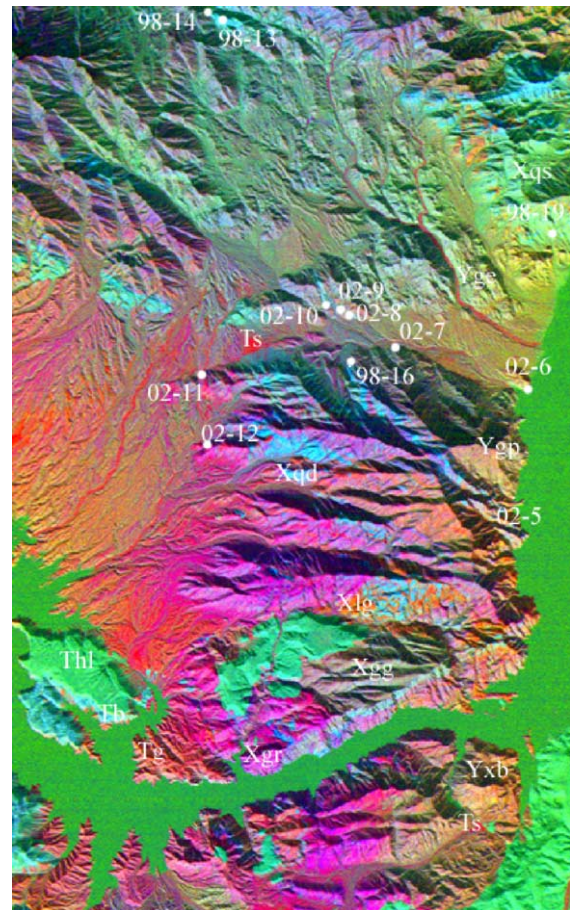


Fig. 8. Decorrelation stretch of MASTER channels 47, 44 and 43 displayed in red, green and blue, respectively for the Hiller Mountains study area. Labels are discussed in text.

In all cases the images were panoramically corrected after processing and prior to production of the final image. Panoramic correction removes the increasing distortion from the center to the edge of the image associated with the change in pixel size due to increasing scan angle.

## 6. Data interpretation

Initially, the results from the Hiller Mountains are described. This discussion includes interpretation of the decorrelation stretch image and the weight percent $SiO_2$ map derived from the MASTER data. This is followed by the equivalent results from the La Reforma caldera region.

### 6.1. Hiller Mountains

Fig. 8 shows a decorrelation stretch image of MASTER channels 47, 44 and 43 displayed in red, green, and blue, respectively. These channels provide the equivalent decor-

relation stretch image to that widely used with TIMS data (e.g. Gillespie et al., 1986). In this image the color change from blue to green to orange to purple to red results from a shift in the emissivity minimum from longer wavelengths (channel 47) to shorter wavelengths (channels 44 and 43) caused by a change in silicate mineralogy. As a result the more mafic rocks appear blue-green and the more felsic rocks purple-red. Areas of limestone (marl) appear green. This image shows considerable compositional variation with discrete mappable units where earlier workers had mapped a single undivided block (Longwell et al., 1965; Volborth, 1962). The imagery, together with field mapping, was used to produce an updated 1:24,000 geologic map for the Hiller Mountains (Fig. 9). The main discernable units within the imagery are described below with an example area highlighted on the image.

The oldest rocks in the area are supracrustal garnet gneisses of Paleoproterozoic age that appear purple to magenta in the decorrelation stretch image (Xgr, Fig. 8). Much of the garnet gneiss is retrograded with the garnets being replaced with chlorite and sericite. Also of Paleo-
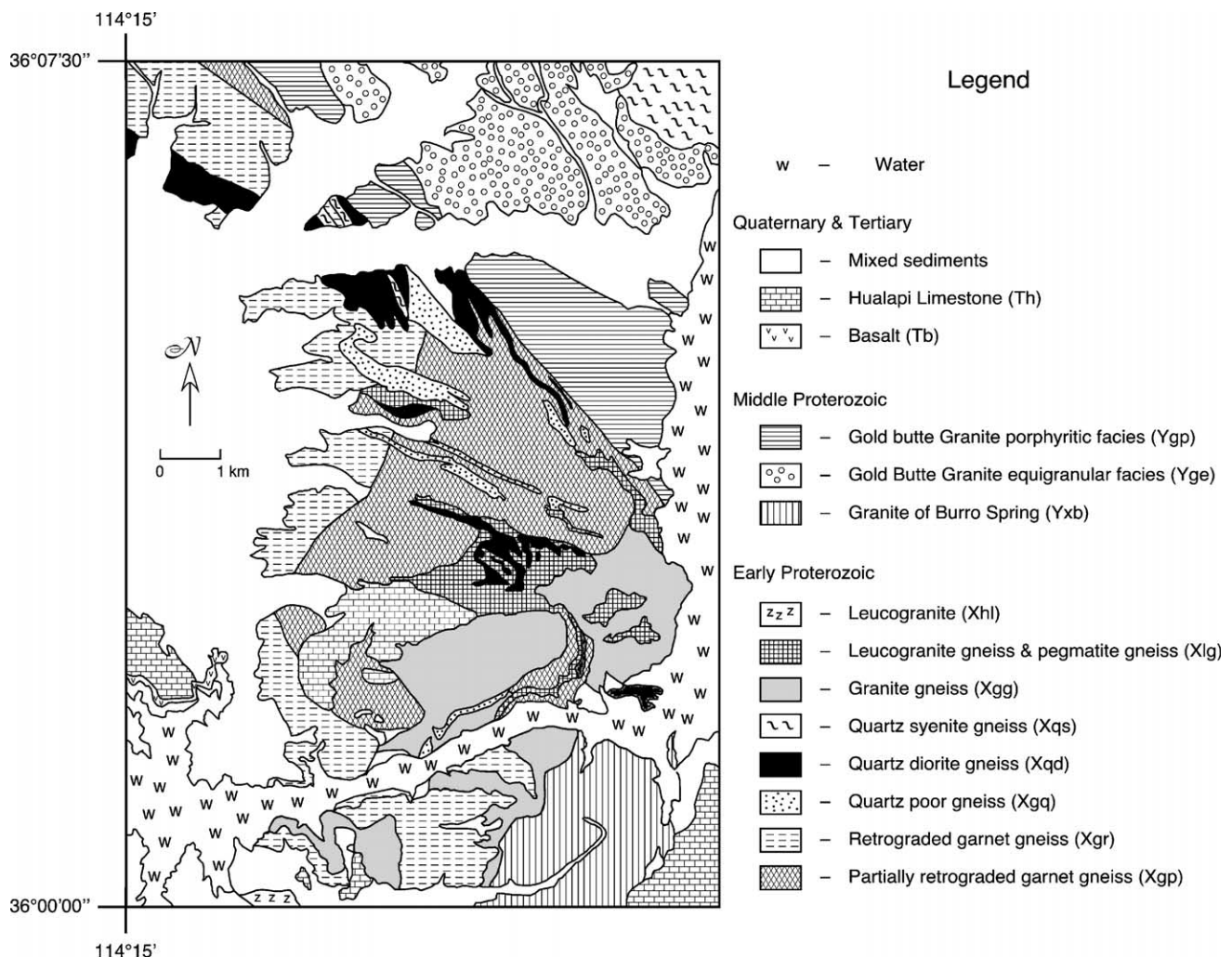


Fig. 9. Simplified geological map of the Hiller Mountains study area. Map based on updated 1:24,000 map sheet for Hiller Mountains (Howard et al., 2003).

proterozoic age are bodies of quartz diorite gneiss, quartz syenite gneiss, granite gneiss and leucogranite gneiss, which appear as blue (Xqd), pale green (Xqs), purple-gray (Xgg), and orange (Xlg), respectively (Fig. 8).

The Mesoproterozoic-age Gold Butte Granite (Ygp, Yge) and the correlative(?) granite of Barrel Spring (Yxb) appear orange, purple, and gray-green and closely resemble each other (Fig. 8). These granites and the older gneisses are unconformably overlain by Miocene sedimentary rocks and volcanic rocks that include basalt, arkosic conglomerate, limestone, and sandstone which appear blue (Tb), orange-red (Tg), green (Thl), and red (Ts), respectively (Fig. 8). The Tertiary sedimentary rocks and volcanic rocks are overlain by gravel, conglomerate, limestone, sandstone, and alluvium of Pliocene and Quaternary age. The colors of these deposits on the image tend to be the same as the colors of the source of the material on the image, and the source material can often be determined from the image. Clearly the updated geological map is in good agreement with the images (Figs. 8 and 9) with the images highlighting mineralogical differences. Because the images relate directly to mineralogy, rocks with similar compositions but different ages appear similar and fieldwork is required to correctly determine the stratigraphy and structural history of the area.

Fig. 10 shows the weight percent silica map derived from the MASTER data for the Hiller Mountains area. The weight percent silica value for a given pixel depends on wavelength position of the minimum of the best fit Gaussian to the emissivity spectrum. The emissivity spectrum represents all the materials present in the pixel and will typically be a mixture of rock, soil and vegetation. Since the emissivity spectrum of vegetation is similar to that of a blackbody, any vegetation present in the pixel will tend to reduce the spectral contrast in the pixel which should not affect the position determined by Gaussian fitting provided sufficient rock/soil is present. Any weathering or soil development will affect the position that is determined since certain minerals will be weathered out from the mixture. In Fig. 10 more mafic rocks, which appear blue and green in the decorrelation stretch image (Fig. 8), are characterized by low weight percent $SiO_2$ values whereas felsic rocks, which appear purple-orange-red in the decorrelation stretch image (Fig. 8), are characterized by high weight percent $SiO_2$ values. The weight percent $SiO_2$ mapping algorithm assigns areas of limestone low silica values because carbonates have an emissivity minimum at long wavelengths in channel 49, slightly beyond the longest wavelength of the silicates exposed in the area. Obviously the weight percent silica estimates for the limestones are incorrect but they do demonstrate that the algorithm has correctly identified a longer wavelength absorption feature.

The weight percent silica map shown in Fig. 10 has considerably more noise than the decorrelation stretch images. The increase in noise compared with the decorrelation stretch data results from both the Gaussian fitting and the need to fit the Gaussian function to the emissivity data.
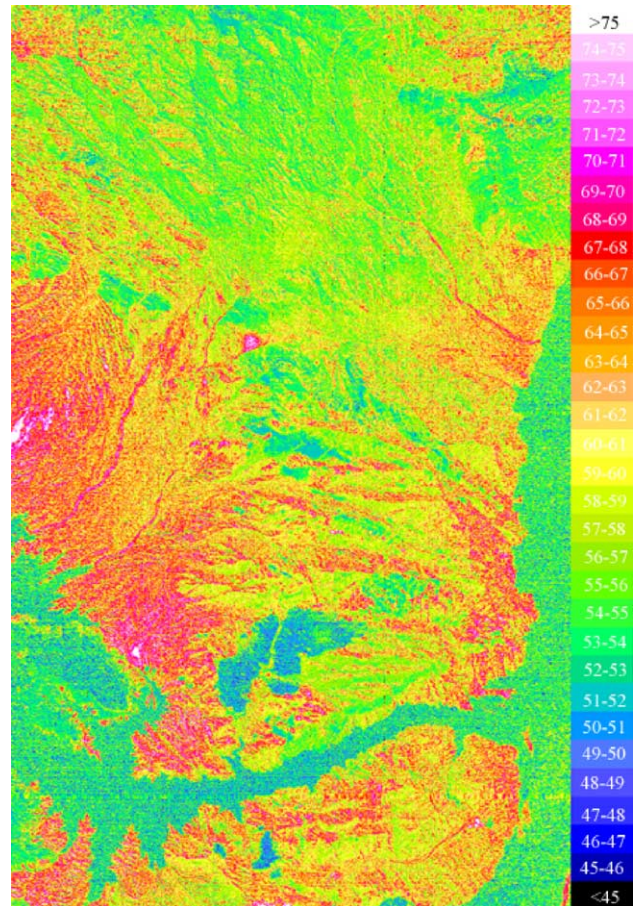


Fig. 10. Weight percent $SiO_2$ map for the Hiller Mountains study area. Key on right hand side indicates weight percent $SiO_2$ associated with a particular color on the image.

Emissivity data contain more noise than the radiance data which are dominated by temperature and utilized by the decorrelation stretch. Further, although the minimum of the Si–O stretching region migrates to longer wavelengths as the weight percent silica decreases, there is some variation between minerals which introduces some scatter in the function used to derive the weight percent silica from the minimum. Although the weight percent silica maps contain more noise, a quantitative comparison of the image estimates with chemical analyses on field samples shows the maps are reasonably accurate, although they can be systematically biased. In order to assess the accuracy of the weight percent $SiO_2$ map, samples were collected from 14 localities, and the weight percent silica of the samples determined by chemical analysis. The average weight percent $SiO_2$ for a $3 \times 3$ block of pixels centered on each sample site on the image was then compared to the results from the chemical analysis of the field samples (Table 4). Examination of this table indicates the largest positive difference (field sample minus image) is 11% and the largest negative difference is 6% with an average error of 2% and standard deviation of 5%. Clearly the weight percent $SiO_2$ retrieved from the image data is, on average, in good

Table 4
Comparison of weight percent $SiO_2$ determined by chemical analysis of field samples and the MASTER data for the Hiller Mountains study area

| Site | Weight percent silica | | | | |
|---|---|---|---|---|---|
| | Laboratory | $N$ samples | Image | Std dev | Difference |
| 98-13a | 50.47 | 2 | 51.76 | 0.37 | −1.29 |
| 98-14a | 66.93 | 1 | 55.91 | 3.98 | 11.02 |
| 98-15a | 48.38 | 1 | 54.36 | 2.19 | −5.98 |
| 98-16 | 49.82 | 1 | 51.89 | 0.51 | −2.07 |
| 98-18 | 49.08 | 1 | 54.17 | 1.26 | −5.09 |
| 98-19a | 58.68 | 1 | 56.42 | 1.02 | 2.26 |
| 02-5 | 71.67 | 1 | 65.56 | 1.64 | 6.11 |
| 02-6 | 68.65 | 1 | 67.32 | 3.1 | 1.33 |
| 02-7 | 67.42 | 1 | 58.35 | 2.71 | 9.07 |
| 02-8 | 51.18 | 2 | 55.65 | 1.12 | −4.47 |
| 02-9 | 62.43 | 1 | 56.81 | 2.74 | 5.62 |
| 02-10 | 56.78 | 2 | 54.80 | 1.51 | 1.98 |
| 02-11 | 66.12 | 2 | 61.23 | 2.19 | 4.89 |
| 02-12 | 69.98 | 2 | 64.74 | 4.18 | 5.24 |

Data from MASTER are averages of 3×3 blocks of pixels centered on the sample location. Standard deviation is the average standard deviation if more than one sample was used.

agreement with the weight percent $SiO_2$ measured from the field samples. However, closer examination indicates the algorithm tends to underestimate weight percent $SiO_2$ values greater than 56% and overestimate weight percent $SiO_2$ values under 56% (Fig. 11). Further work is needed to determine the exact cause of this behavior, but instrument calibration problems, incomplete atmospheric correction, particle size, packing and weathering are possible candidates. Weathering could cause this effect by adding soil to the response from the pixel, but not in the laboratory reference curve. The clay component of the soil will tend to shift the high silica values to lower silica values and the low silica values to higher values because the main absorption feature for clays is between 9.5 and 10 μm. Regardless of

the cause, the effect can be removed by obtaining a correction from the regression of the field values to the image values. The application of the correction to these data is shown in Fig. 12. This correction also improves the fit of the data from the Tres Virgenes-La Reforma study site suggesting a systematic error, but a still better result can be obtained from the Tres Virgenes-La Reforma site using local samples.

The map patterns revealed in the Proterozoic rocks by the new imaging and mapping carry regional structural and petrologic significance. The older garnet gneisses are derived from supracrustal protoliths. The high abundance and petrologic diversity of metaplutonic units is greater than described in nearby areas and suggests that this area records a rich and dateable history of Proterozoic plutonism and crust building for this part of the Mojave crustal province. Compositions vary from ultramafic and gabbroic to granitic, and include homogeneous plutons of distinctive spectral response as subunits of granite gneiss. The quartz syenite gneiss unit is unusual in composition compared to most other Paleoproterozoic synorogenic igneous rocks in the southwestern United States, which mostly are calc-alkaline as is typical of orogenic belts. The quartz syenite gneiss forms a pluton and small bodies characterized by perthite and microcline megacrysts, biotite, and little quartz. It was identified by Volborth (1962), and the difference in chemistry was clearly apparent in the MASTER imagery. The ability to remotely map chemical variations offers the possibility of quantifying subtle changes in the chemical composition of the areas of Proterozoic rocks. The intricate map patterns demonstrate continuity of the crystalline rocks from the Gold Butte block southward into the Hiller Mountains and beyond into the White Hills, thereby supporting the idea that these ranges represent an essentially continuous footwall block below a regional detachment
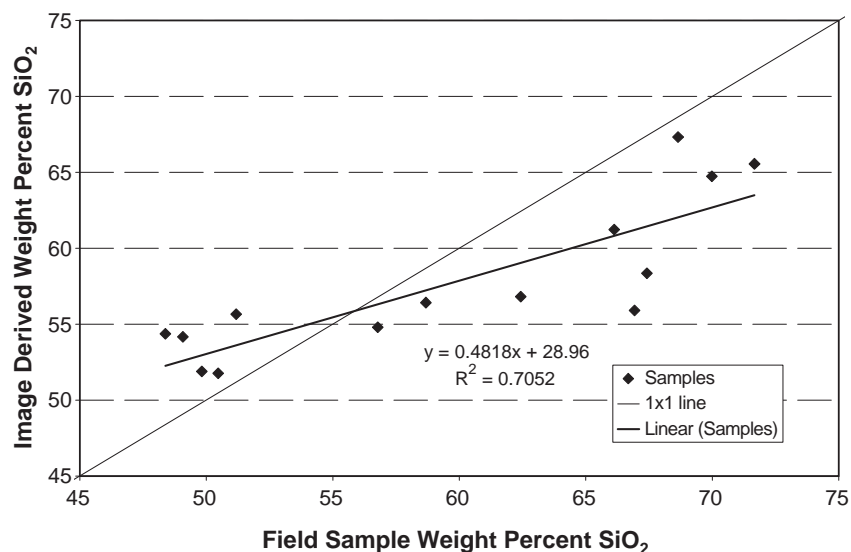


Fig. 11. Plot of weight percent $SiO_2$ values derived from the image for selected field sites versus similar values derived from samples collected from the field sites.
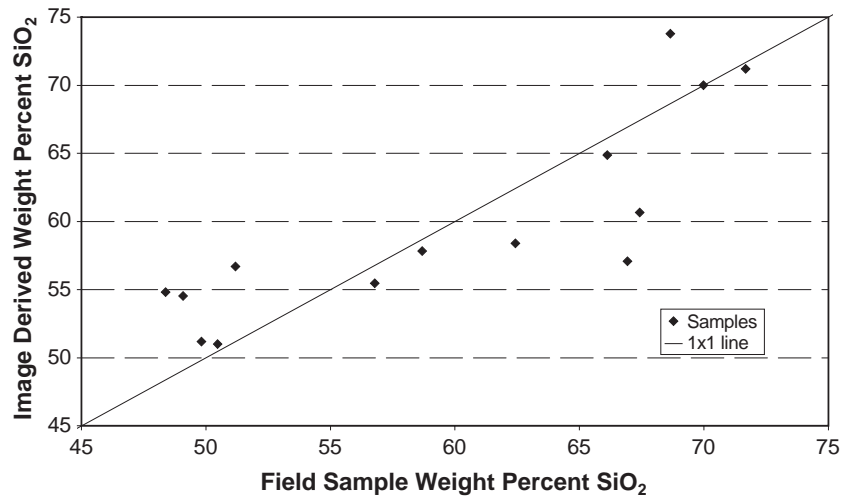
Fig. 12. Plot of weight percent $SiO_2$ values derived from the image for selected field sites versus similar values derived from samples collected from the field sites after terrain adjustment. The formula for the terrain adjustment was $y=mx+c$ where $m=1.464$ and $c=-24.752$.

fault (Duebendorfer & Sharp, 1998; Fryxell et al., 1992). Mapped irregular contacts of plutonic and metamorphic rocks show apparent small left-lateral separations across Virgin Canyon and across Jumbo Pass, suggestive of several concealed small-displacement east-striking faults. One such fault offset exposed on the north side of Jumbo Pass, that was identified from the imagery. Field checking of this fault revealed that it dips northward 30–50° and exhibits northwest-trending slickenlines indicative of left-normal oblique displacement. The newly recognized family of east-striking left-separation faults resembles and may relate to either or both of two sets of regional Miocene-age faults: (1) WNW-dipping down-to-west normal faults that offset the Paleozoic rocks capping the Gold Butte block in a series of left-separation steps (Brady et al., 2000), and (2) the northeast-striking left-lateral faults that are present 20–40 km north and northwest of the Hiller Mountains (Anderson, 1973; Duebendorfer et al., 1998).

### 6.2. La Reforma Caldera region

Fig. 13 shows a decorrelation stretch image of MASTER channels 47, 44 and 43 displayed in red, green and blue, respectively. Fig. 14 shows a geologic map of the area based on Schmidt (1975) and Demant (1984), with revisions from field mapping and image analysis. The mapped units can be distinguished in the decorrelation stretch (Fig. 13); however, due to the low altitude acquisition of these data (2 km), tilting and pitching of the aircraft have warped the image considerably. The image shown in Fig. 13 is a 5 km by 3 km region (eastern flank) of the La Reforma caldera. Included are a recent scoria cone, a portion of the intracaldera sequence of ash flow tuffs and lavas, and an intrusive diorite porphyry.
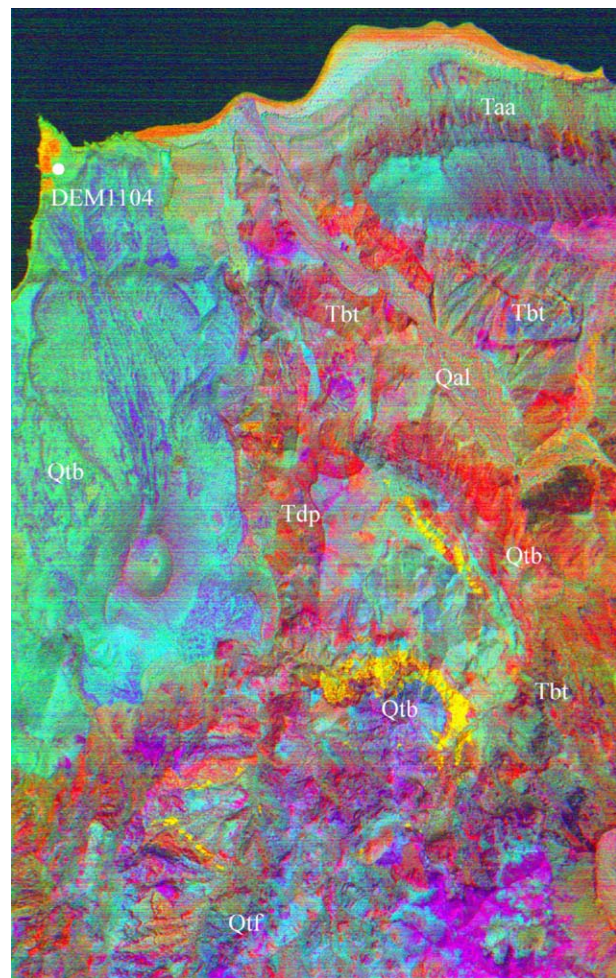


Fig. 13. Decorrelation stretch of MASTER channels 47, 44 and 43 displayed in red, green and blue, respectively for the La Reforma Caldera study area. Labels are discussed in text.
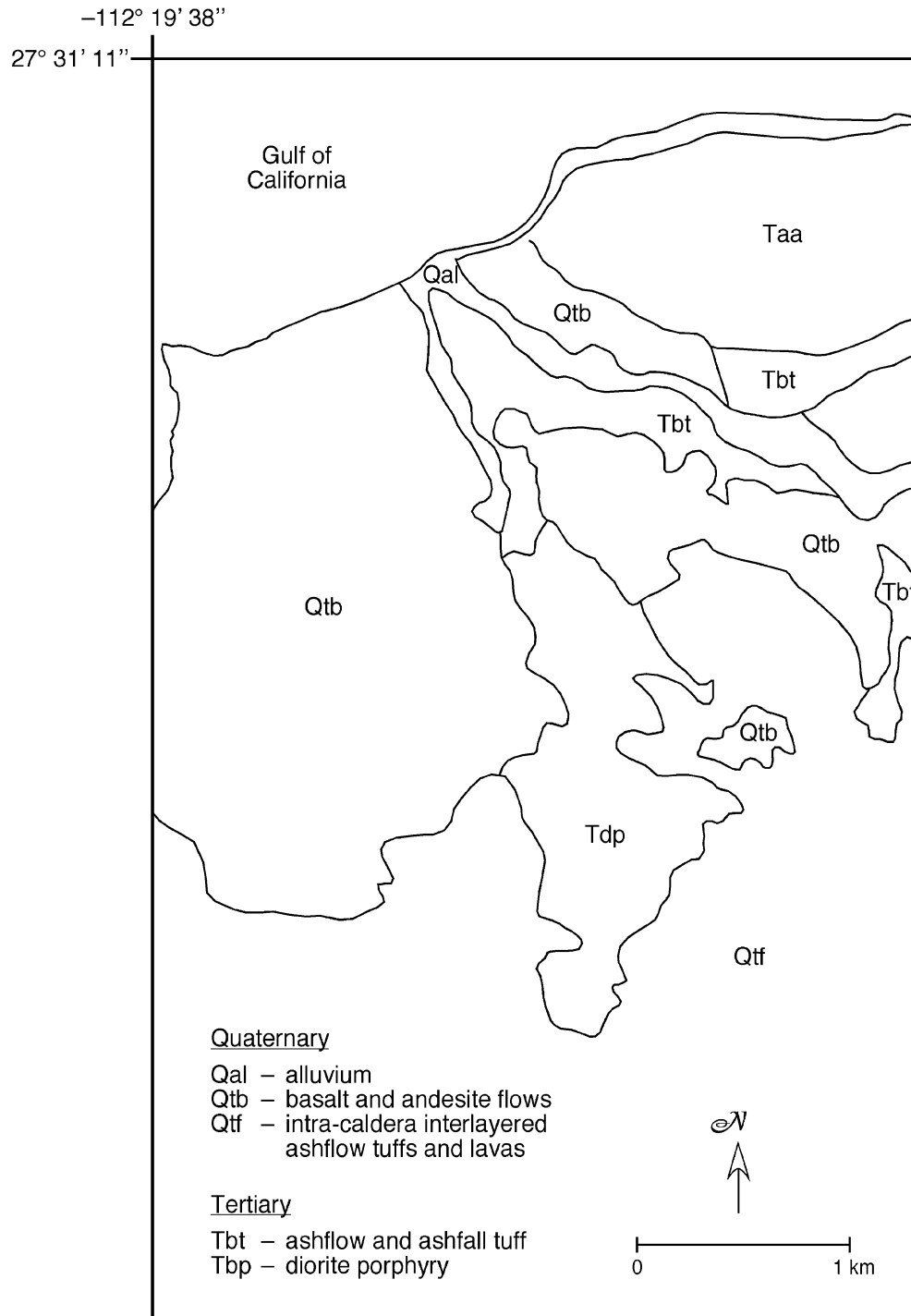
Fig. 14. Simplified geological map of the La Reforma Caldera study area. Map based Schmidt (1975) and Demant (1984) with field revisions.

The oldest rocks in Fig. 13 are highly weathered porphyritic diorite intrusives of Tertiary age which appear as various colors from orange to purple in the decorrelation stretch image (Tdp, Fig. 13). Due to the high degree of weathering of this unit, the surface composition is fairly diverse, rendering this unit difficult to discriminate in the decorrelation stretch image. Also of Tertiary age are the ash flow, ash fall, and pumice fall tuffs associated with the pre-collapse explosive products of the caldera, which appear as orange and green (Tbt) (Fig. 13). The intracaldera sequence of interlayered ash flow tuffs and lavas (Qtf) appears pink in the decorrelation stretch. The Quaternary-age basaltic–andesite flows (Qtb) appear blue and green (Fig. 13). However, part of this unit (directly below the Qtb symbol) is bright red in the decorrelation stretch (Fig. 13) and the weight percent silica map (Fig. 15). Previously believed to be of mafic to intermediate composition; this apparently more silicic composition warrants further investigation and

may indicate that additional revisions are necessary to update the geologic map. The Quaternary sediments appear reddish-orange along the coastline but are of mixed color within the arroyo, indicating less weathering and sorting has occurred in this location. The updated geological map is in moderate agreement with the images (Figs. 13 and 14), with the images highlighting mineralogical differences.

Seven samples were collected from the area covered by the Baja image data to calibrate silica percentage maps. Additionally, one weight percent silica measurement was obtained from a published report by Demant (1984). The 7 sample sites are located outside the image area of Fig. 13, but were taken from similar volcanic assemblages in the La Reforma caldera region. The weight percent silica of the samples was determined by chemical analysis. The average weight percent $SiO_2$ for a $3\times3$ block of pixels centered on each sample site on the image was then compared to the results from the chemical analysis of the field samples (Table 5). Examination of this table indicates the largest positive difference (field sample minus image) is 14.08% and the largest negative difference is .02% with an average error of 6.5% and standard deviation of 5.6%. Examination of Table 4 indicates the algorithm tends to slightly

Table 5
Comparison of weight percent $SiO_2$ determined by chemical analysis of field samples and the MASTER data for the La Reforma Caldera

| Site | Lab | Image (standard fit) | Lab minus image (standard fit) | Image (scene fit) | Lab minus image (scene fit) |
|------|-------|-------|--------|-------|-------|
| VC8959 | 74.00 | 60.67 | 13.33 | 75.04 | −1.04 |
| MT9167 | 58.08 | 53.86 | 4.22 | 59.28 | −1.20 |
| VC8966 | 74.75 | 60.67 | 14.08 | 75.04 | −0.29 |
| 3V9027 | 65.85 | 54.23 | 11.62 | 60.16 | 5.69 |
| 3V9028 | 51.04 | 51.24 | −0.20 | 53.23 | −2.19 |
| SAW350 | 57.70 | 52.24 | 5.46 | 55.55 | 2.15 |
| SAW103 | 52.67 | 51.60 | 1.07 | 54.05 | −1.38 |
| DEM1104 | 55.56 | 53.00 | 2.56 | 57.30 | −1.74 |

Of the samples only one occurs in the area covered in the images presented (DEM1104). Data from MASTER are averages of $3\times3$ blocks of pixels centered on the sample location. Standard fit refers to when the coefficients used in the equation that relates the minimum of the spectrum to the weight percent silica were taken from Table 1 MASTER channels 42–49. Scene fit refers to the custom equation developed for the La Reforma dataset that relates the minimum in the field samples taken from the area to the minimum observed in the image data.

overestimate weight percent $SiO_2$ values for rocks with low weight percent $SiO_2$ and underestimate the weight percent $SiO_2$ of rocks with high weight percent SiO2 values. As discussed earlier, there are several possible causes for this difference and further work is needed to evaluate them but in the interim the effect can be removed by regressing to local field samples. The application of the correction to these data is shown in Fig. 15.

The map patterns in Figs. 13 and 15 revealed highly variable weathered porphyritic diorite ash flow tuffs and lavas to the west (in the center of the caldera) and more recent basaltic–andesite flows to the east, on the flank of the caldera. This supports the theory by Demant (1984) that the rising mafic magma, associated with the current tectonics of continental extension in the area, is blocked from rising in the interior of the caldera due to a molten, shallow reservoir beneath the caldera. Thus, the recent basaltic–andesite flows only erupt on the caldera's flanks. A scoria cone similar to the one shown in Fig. 13 is found on the southeastern flank of the caldera as well.

## 7. Summary and conclusions

Multispectral thermal infrared images were acquired from two sites: Hiller Mountains, Nevada, USA and Tres Virgenes-La Reforma, Baja California Sur, Mexico. These data were used to test an improved technique for remotely estimating the weight percent $SiO_2$ of silicate rocks exposed on the surface. The technique uses laboratory emissivity data from spectral libraries to develop a relationship between the known shift in the minimum in the Si–O stretching region to longer wavelengths and decreasing weight percent $SiO_2$. This relationship is then applied to the emissivity data extracted from the images. The relationship was shown to depend on
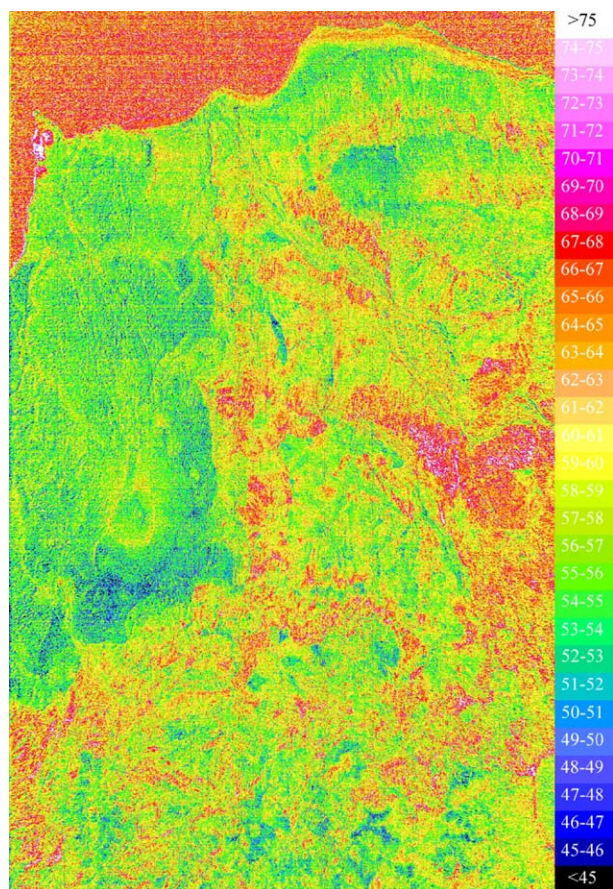


Fig. 15. Weight percent $SiO_2$ map for the La Reforma Caldera study area. Key on right hand side indicates weight percent $SiO_2$ associated with a particular color on the image.

how well the emissivity data encompass the Si–O stretching region. Different relationships were developed for various channel combinations as well as instruments. The channel combinations were selected to include the wavelength region that can be readily corrected for atmospheric effects typically encountered with airborne and spaceborne terrestrial thermal infrared data.

The results indicate that using the relationship developed from the library data with the images that the image derived weight percent $SiO_2$, on average agrees with the field samples to better than 2% for the Hiller Mountains study area and better than 7% for the Tres Virgenes-La Reforma area. However, the library-derived algorithm tends to underestimate high weight percent silica values and over-estimate low weight percent silica values. The exact cause for the underestimation was not determined but likely results from the image pixels consisting of a mixture of materials compared to library samples. Future work will investigate the cause of this difference but the difference can be corrected based on the availability of a few samples from the study region.

Interpretation of the thermal infrared data from the Hiller Mountains suggests the region contains an unusually diverse range of Proterozoic petrologic units and the area would be well suited for further study to determine the history of Proterozoic plutonism and crust building for this part of the Mojave crustal province.

Examination of the weight percent silica maps for the Baja California data suggests the intracaldera products are highly varied products of mafic to silicic eruptions. The more recent volcanic products on the flanks of the caldera are of mafic to intermediate composition. It should be noted, however, that a portion of the mapped unit Qtb, Quaternary basaltic–andesite flows, may be more silicic than previously described (Demant, 1984; Schmidt, 1975).

In both study areas, the thermal infrared images allow the discrimination of previously unmapped geological units/structures. They also allowed quantitative estimates of the weight percent silica of certain units and revealed greater compositional variation than indicated on previous geological maps. The images used in conjunction with conventional fieldwork allowed the rapid production of detailed geological maps of previously poorly mapped areas.

## Acknowledgements

## References

Abrams, M. J., Abbott, E. A., & Kahle, A. B. (1991). Combined use of visible, reflected infrared and thermal infrared images for mapping Hawaiian lava flows. *Journal of Geophysical Research*, *96*, 475–484.

Anderson, J. L. (1983). Proterozoic anorogenic granite plutonism of North America. *Geological Society of America Memoir*, *161*, 133–154.

Anderson, R. E. (1973). Large-magnitude late tertiary strike-slip faulting north of Lake Mead, Nevada. *U.S. Geological Survey Professional Paper*, *794–818*.

Bandfield, J. L. (2002). Global mineral distributions on Mars. *Journal of Geophysical Research-Planets*, *107*, E6.

Beard, L. S. (1996). Paleogeography of the Horse Spring Formation in relation to the Lake Mead fault system, Virgin Mountains, Nevada and Arizona. *Special Paper-Geological Society of America*, *303*, 27–59.

Berk, A., Bernstein, L. S., & Robertson, D. C. (1989). *MODTRAN: a moderate resolution model for LOWTRAN 7, AFGL-TR-89-0122*. Bedford, MA: Air Force Geophysics Laboratory.

Bernet, M., Brandon, M., Garver, J., Reiners, P., & Fitzgerald, P. G. (2002). Determining the zircon fission-track closure temperature. *Abstracts with Programs-Geological Society of America*, *34*, A-18.

Brady, R., Wernicke, B., & Fryxell, J. (2000). Kinematic evolution of a large-offset continental normal fault system, South Virgin Mountains, Nevada. *Geological Society of America Bulletin*, *112*, 1375–1397.

Chamberlain, K. R., & Bowring, S. A. (1990). Proterozoic geochronology and isotopic boundary in NW Arizona. *Journal of Geology*, *98*, 399–416.

Colletta, B., & Angelier, J. (1981). Faulting evolution of the Santa Rosalia Basin, Baja California, Mexico. In L. Ortlieb, & O. Roldan (Eds.), *Geology of Northwestern Mexico and Southern Arizona. UNAM-Hermosillo/Sonora* (pp. 265–274).

Cudahy, T. J., Whitbourn, L. B., Conner, P. M., Mason, P., & Phillips, R. N. (1999). Mapping surface mineralogy and scattering behavior using backscattered reflectance from a hyperspectral midinfrared airborne $CO_2$ laser system (MIRACO(2)LAS). *IEEE Transactions on Geoscience and Remote Sensing*, *37*, 2019–2034.

Demant, A. (1984). *The La Reforma caldera, Santa Rosalia area, Baja California, a volcanological, petrological and mineralogical study: Neotectonics and sea level variations in the Gulf of California area, a symposium* (pp. 77–96). Mexico, DF: Univ. Nal. Auton Mexico, Inst. Geologia.

Demant, A., & Ortlieb, L. (1981). Plio-pleistocene volcano-tectonic evolution of La Reforma Caldera, Baja California, Mexico. *Tectonophysics*, *71*, 194.

Duebendorfer, E. M., Beard, L. S., & Smith, E. I. (1998). Restoration of Tertiary deformation in the Lake Mead region, southern Nevada. The role of strike-slip transfer faults. *Special Paper-Geological Society of America*, *323*, 127–148.

Duebendorfer, E. M., Chamberlain, K. R., & Jones, C. S. (2001). Paleoproterozoic tectonic history of the Cerbat Mountains, northwestern Arizona: Implications for crustal assembly in the southwestern United States. *Geological Society of America Bulletin*, *113*, 575–590.

Duebendorfer, E. M., & Sharp, W. D. (1998). Variation in displacement along strike of the South Virgin-White Hills detachment fault: Perspective from the Northern White Hills, Northwestern Arizona. *Geological Society of America Bulletin, 110*, 1574–1589.

Fitzgerald, P. G., Fryxell, J. E., & Wernicke, B. P. (1991). Apatite fission track constraints on the extensional evolution of the Gold Butte crustal section, South Virgin Mountains, Nevada. *Geology, 19*, 1013–1016.

Fryxell, J. E., Salton, G. G., Selverstone, J., & Wernicke, B. (1992). Gold Butte crustal section, South Virgin Mountains, Nevada. *Tectonics, 11*, 1099–1120.

Gillespie, A., Rokugawa, S., Matsunaga, T., Cothern, S., Hook, S., & Kahle, A. (1998). Temperature and emissivity separation algorithm for advanced spaceborne thermal emission and reflectance radiometer (ASTER) images. *Geoscience and Remote Sensing, 36*, 1113–1126.

Gillespie, A. R. (1986). Lithologic mapping of silicate rocks using TIMS. *Proceedings of the thermal infrared multispectral scanner data user's workshop, jet propulsion laboratory publication 86-38* (pp. 29–44). Pasadena, CA: Jet Propulsion Laboratory, California Institute of Technology.

Gillespie, A. R. (1992). Spectral mixture analysis of multispectral thermal infrared images. *Remote Sensing of Environment, 42*, 137–145.

Gillespie, A. R., Kahle, A. B., & Walker, R. E. (1986). Color enhancement of highly correlated images: I. Decorrelation and HSI contrast stretches. *Remote Sensing of Environment, 20*, 209–235.

Guerrero-Guadarrama, J. L. (1998). Actividad Sísmica del Campo Geotérmico de Las Tres Virgenes, B.C.S., México. *Geotermia, 14*, 87–100.

Hausback, B. P., Stock, J. M., Dmochowski, J. E., Farrar, C. D., Fowler, S. J., Sutter, K., Verke, P., & Winant, C. (2000). To be or not be a caldera—La Reforma caldera, Baja California Sur, Mexico. *Program with Abstracts-Geological Society of America, 32*, A502.

Hawkins, D., Bowring, S. A., Ilg, B., Karlstrom, K. E., & Williams, M. L. (1996). U–Pb geochronologic constraints on Paleoproterozoic crustal evolution, Upper Granite Gorge, Grand Canyon, Arizona. *Geological Society of America Bulletin, 108*, 1167–1181.

Hook, S. J., Gabell, A. R., Green, A. A., & Kealy, P. S. (1992). A comparison of techniques for extracting emissivity information from thermal infrared data for geologic studies. *Remote Sensing of Environment, 42*, 123–135.

Hook, S. J., Karlstrom, K. E., Miller, C. F., & McCaffrey, K. J. W. (1994). Mapping the Piute Mountains, CA with thermal infrared multispectral scanner (TIMS) data. *Journal of Geophysical Research, 99*, 15605–15622.

Hook, S. J., Myers, J. J., Thome, K. J., Fitzgerald, M., & Kahle, A. B. (2001). The MODIS/ASTER airborne simulator (MASTER)—a new instrument for earth science studies. *Remote Sensing of Environment, 76*, 93–102.

Howard, K. A., Hook, S. J., Phelps, G. A., Block, D. L., (2003), Geologic map of the Hiller Mountains Quadrangle, Clark County, Nevada and Mohave County, Arizona: Nevada Bureau of Mines and Geology Map 137, scale 1:24,000. http://www.nbmg.unr.edu/dox/m137plate.pdf

Hunt, G. R. (1980). Electromagnetic radiation: The communication link in remote sensing. In B. S. Siegal, & A. R. Gillespie (Eds.), *Remote sensing in geology* (pp. 5–45). New York: John Wiley.

Ilg, B., Karlstrom, K. E., Hawkins, D., & Williams, M. L. (1996). Tectonic evolution of paleoproterozoic rocks in Grand Canyon, insights into middle crustal processes. *Geological Society of America Bulletin, 108*, 1149–1166.

Lahren, M. M., Schweickert, R. A., & Taranik, J. V. (1988). Analysis of the northern Sierra accreted terrain, California, with airborne thermal infrared multispectral scanner data. *Geology, 16*, 525–528.

Longwell, C. R., Pampeyan, E. H., Bowyer, B., & Roberts, R. J. (1965). Geology and mineral deposits of Clark County, Nevada. *Bulletin-Nevada Bureau of Mines, 62*, 126–133.

Mammerickx, J., & Kiltgord, K. D. (1982). Northern east pacific rise: Evolution from 25 m.y.b.p. to the present. *Journal of Geophysical Research, 87*, 6751–6759.

Neville, R. A., Levesque, J., Staenz, K., Nadeau, C., Hauff, P., & Borstad, G. A. (2003). Spectral unmixing of hyperspectral imagery for mineral exploration: Comparison of results from SFSI and AVIRIS. *Canadian Journal of Remote Sensing, 29*, 99–110.

Plaza, A., Martinez, P., Perez, R., & Plaza, J. A. (2004). A quantitative and comparative analysis of endmember extraction algorithms from hyperspectral data. *IEEE Transactions on Geoscience and Remote Sensing, 42*, 650–663.

Ramsey, M. S., & Christensen, P. R. (1998). Mineral abundance determination: Quantitative deconvolution of thermal emission spectra. *Journal of Geophysical Research-Solid Earth, 103*, 577–596.

Reiners, P. W. (2002). (U–Th)/He chronometry experiences a renaissance. *Eos, American Geophysical Union Transactions, 83*, 21–27.

Reiners, P. W., Brady, R., Farley, K. A., Fryxell, J. E., Wernicke, B., & Daniel, L. (2000). Helium and argon thermochronometry of the Gold Butte block, South Virgin Mountains, Nevada. *Earth and Planetary Science Letters, 178*, 315–326.

Sabine, C., Realmuto, V. J., & Taranik, J. V. (1994). Quantitative estimation of granitoid composition from thermal infrared multispectral scanner (TIMS) data, Desolation Wilderness, northern Sierra, Nevada, California. *Journal of Geophysical Research, 99*, 4261–4271.

Sawlan, M. G. (1988). Late Cenozoic volcanism in the Tres Virgenes area. In L. Ortlieb, & J. Roldan-Q. (Eds.), *Geology of northwestern Mexico and southern Arizona: Field guides and papers* (pp. 309–319). Geol. Soc. Am. Cordilleran Section, 1981 Annual Meeting, Hermosillo.

Sawlan, M. G. (1986), Petrogenesis of late Cenozoic volcanic rocks from Baja California Sur, PhD dissertation, University of California, Santa Cruz, CA.

Sawlan, M. G., & Smith, J. G. (1984). Late Cenozoic volcanic suites in northern Baja California Sur, Mexico: Their relations to subduction and rifting along the Baja California peninsula (abs.). *Program with Abstract-Geological Society of America, 16*, 645.

Schmidt, E. K. (1975), Plate tectonics, volcanic petrology and ore formation in the Santa Rosalia area, Baja California, Mexico, master's thesis, University of Arizona.

Thomas, W. M., Clark, H. S., Young, E. D., Orell, S. E., & Anderson, J. L. (1988). Proterozoic high-grade metamorphism in the Colorado River region, Nevada, Arizona, and California. In W. G. Ernst (Ed.), *Metamorphism and rustal evolution of the Western United States* (pp. 526–537). Englewood Cliffs, NJ: Prentice Hall.

Volborth, A. (1962). Rapakivi-type granites in the Precambrian complex of Gold Butte, Clark Country, Nevada. *Geological Society of America Bulletin, 73*, 813–832.

Walker, G. P., Jurado, Z., Rowland, S., & Carrillo, A. (1992). La Reforma cryptodome: An alternative mechanism to caldera subsidence and resurgent doming. *29th international geological congress meeting, Kyoto, Japan* (p. 481).

Watson, K., Rowan, L. C., Bowers, T. L., Anton-Pacheco, C., Gumiel, P., & Miller, S. H. (1996). Lithologic analysis from multispectral thermal infrared data of the alkalic rock complex at Iron Hill, Colorado. *Geophysics, 61*, 706–721.

Wernicke, B., & Axen, G. J. (1988). On the role of isostasy in the evolution of normal fault systems. *Geology, 16*, 848–851.

Wernicke, B., Guth, P. L., & Axen, G. J. (1984). Tertiary extensional tectonics in the Sevier thrust belt of southern Nevada. *Geological society of America annual meeting guidebook N. 4, field trip 19* (pp. 473–510). Reno, Nevada: McKay School of Mines.

Wooden, J. L., & Miller, D. M. (1990). Chronologic and isotopic framework for early Proterozoic crustal evolution in the eastern Mojave Desert region, SE California. *Journal of Geophysical Research, 95*, 20133–20146.